行政院國家科學委員會專題研究計畫 期中進度報告

膜過濾結垢機制及預防之研究--薄膜生物顆粒反應器新程序之開發及機制(2/3)
期中進度報告(精簡版)

計 畫 類 別 ： 整合型
計 畫 編 號 ： NSC 95-2221-E-002-385-
執 行 期 間 ： 95 年 08 月 01 日至 96 年 07 月 31 日
執 行 單 位 ： 國立臺灣大學化學工程學系暨研究所

計 畫 主 持 人 ： 李篤中

報 告 附 件 ： 國外研究心得報告
出席國際會議研究心得報告及發表論文

處 理 方 式 ： 期中報告不提供公開查詢

中 華 民 國 96 年 04 月 28 日

膜過濾結垢機制及預防之研究－薄膜生物顆粒反應器新程序之開發及機制(2/3)

Process Development and Mechanisms of Membrane-Granule Process

計畫編號：NSC 95-2221-E-002-385

李篤中
國立台灣大學化學工程學系

I. 中文摘要

在本三年計畫中我們將發展二種探測生物絮聚體結構及輸送程序之關鍵技術。在本年計畫中，我們將以第一年計畫中建立之技術針對生物膠羽、好氧顆粒、生物膜 活/死菌及生物間質(EPS)分佈進行測量，及量測其氧濃度之內部動態變化，最後建立分佈與動態變化之關連性。

關鍵詞： 好氧顆粒, 氧, 擴散係數, 結構

Abstract

The structure of fouling layer determines the pressure drop across the fouling layer. Three-dimensional distributions of nucleic acids, proteins, α-D-glucopyranose polysaccharides, β-D-glucopyranose polysaccharides and lipids in the biofouling layer that is formed on a mixed cellulose ester membrane were determined using a six-fold staining protocol combined with confocal laser scanning microscopy (CLSM). Based on the three-dimensional volumetric grid model of the fouling layer structure observed from the series of CLSM images, the intra-layer flow field during filtration was simulated using commercial software. The effective permeability of the fouling layer was estimated to be 2.65×10^{-12} m^2, which determines the upper estimate on the permeability of the fouling layer. The pores were categorized according to their diameters, using the maximum convex perimeter approach, and then the effects of the blocking pores on the permeability of the fouling layer were investigated. Blocking the large pores that accounted for 15% of the porosity reduced the mean permeability by 58%.

Keywords: fouling layer, structure, staining, CLSM, modeling, pore blockage

II. Introduction (緣由與目的)

Membrane fouling reduces the flux and increases the pressure drop across the membrane, causing operational problems and even membrane failure [1]. Le-Clech *et al.* [2] comprehensively reviewed the literature on membrane fouling. Extracellular polymeric substances (EPSs) have been identified as the principal foulants in membrane bioreactor (MBR) processes [3-11]. Rojas *et al.* [12] identified a ten-fold increase in the specific resistance of membranes as the protein concentrations are increased from 30 to 100 mg l^{-1}. Lee *et al.* [13] determined that the supernatant was responsible for up to 37% of the total resistance during membrane filtration. However, Bouhabila *et al.* [14] demonstrated that the total resistance to filtration by the supernatant was 76%. Wisniewski and Grasmick [15] attributed roughly half of the total resistance to filtration to soluble microbial products (SMP) in the supernatant. Lee *et al.* [16] stated that attached cells and SMPs generated a dynamic membrane on the surface of filter membrane. Cho et al. [17] noted that membrane fouling was substantial when the extracted amount of EPS ranged 20-80 mg g^{-1} MVLSS.

The structure of a thin, deposited layer on a filter membrane has been modeled as a homogeneous porous medium with fixed characteristics [18,19]. High performance size exclusion chromatography (HPSEC) has been used to characterize the EPS extracted from various treatment plants, revealing proteins with MW 45-670 kDa and carbohydrates with MW 0.5-1 kDa [20,21]. Nagaoka and Nemoto [22] found that EPS with a molecular weight of over 1000 kDa was responsible for most of the fouling of the membrane. However, the carbohydrate level in SMP is correlated with the fouling potential of the membranes [23-26].

Fluorescently labeled stains were employed to analyze the cells and EPS distributions in biofilms [27-29]. Lee *et al.* [30] probed the cells, polysaccharides and proteins in the biofilm using the following three stains; SYBR Green I, fluorescently labeled lectins and Hoechst 2495. Chen *et al.* [31] was the first to profile the distributions of proteins, α-D-glucopyranose polysaccharides and β-D-glucopyranose polysaccharides in a fouling layer on a filter membrane. A later study elucidated the structure of the biofouling layer using a quadruple staining scheme (nucleic acids, proteins, α- and β-D-glucopyranose polysaccharides) [32] by a series of confocal laser scanning microscopy (CLSM) images of the fouling layer that was converted to bileveled images, from which three-dimensional volumetric grid models of the structure of the fouling layer were generated.

Membrane fouling is a common phenomenon in membrane separation processes. The present work employed a novel six-color staining procedure to probe the distributions of proteins, cells (total and dead), α- and β-D-glucopyranose polysaccharides and lipids in a fouling layer on a membrane surface. The three-dimensional volumetric grid model thus developed was utilized to study the intra-layer flow field in the biological fouling layer using commercial software. The effects of pore blockage on the permeability of the fouling layer were simulated using the detailed structural model. The purpose of this work was to demonstrate a potentially useful tool for building up a structural model of biofouling layer on membrane and for realizing the yielded intra-layer flow field and cross-layer

pressure drop. This scheme can be applied on, but is not limited to, study of biofouling in a running MBR.

III. Experimental (實驗方法)

Sample

Waste activated sludge was obtained from a wastewater treatment plant owned by Presidential Enterprise Corp., Taiwan, which treats 250 m^3 of food-processing wastewater daily using primary, secondary and tertiary treatments. The sludge pH was approximately 6.84. The chemical oxygen demand (COD) of the sludge and filtrate passing through 0.45-μm membrane was 16,000 mg l^{-1} (TCOD) and 86.7 mg l^{-1} (SCOD), respectively, as determined using a spectrometer (DR/2000, HACH, USA). The elemental composition of the dried samples, determined by an elemental analyzer (Perkin-Elmer 2400 CHN) was C, 41.3%; H, 6.6%; and, N, 5.4%.

The sludge supernatant obtained after 30 min of settling was used as the test sample. Flocs were removed to determine the contribution of the colloidal fractions in the supernatant to resistance of the fouling layer. Dead-end membrane filtration tests of obtained supernatant samples were performed in a 30 cm-Hg vacuum using a 0.45μm mixed cellulose and ester membrane (Advantec MFS, Inc., CA, USA). The membrane and fouling layer were carefully removed from the filtration chamber under fully hydrated conditions for further processing.

Staining and imaging

Calcofluor white was purchased from Sigma (St. Louis, USA). FITC, Con A conjugated with tetramethylrhodamine, SYTO 63, SYTOX blue and Nile red were from Molecular Probes (Carlsbad, CA, USA).

During staining, SYTO 63 (20 μM) was initially dipped on the sample (10 drops) and placed on a shaker table for 30 min. Then, 0.1 M sodium bicarbonate buffer (pH 8.8) was added to the sample to maintain the amine group in non-protonated form. Then, the FITC solution (10 g l^{-1}) was added to the sample (10 drops) for 1 h at room temperature. Subsequently, the Con A solution (250 mg l^{-1}, 10 drops) was added to the sample and incubated for another 30 mins. Calcofluor white (fluorescent brightener 28, 300 mg l^{-1}, 10 drops) was then adopted to stain the β-linked D-glucopyranose polysaccharides for 30 mins. In the next step, the Nile Red solution (10 mg l^{-1}, 10 drops) was applied to the sample for 10 mins. After each of the aforementioned five staining stages, the stained sample was washed twice to remove extra stain using phosphate-buffered saline (PBS) at pH 7.4. The stained sample was stored at 4°C. Before observation, the SYTOX Blue solution was added to the samples (10 drops) for incubation for 5 mins.

The stained samples were embedded for cryosectioning and frozen at -20°C, after which 60μm sections were cut on a cryomicrotome and mounted on the microscopic slides for observation.

Confocal laser scanning microscopy (CLSM; Leica TCS SP2 Confocal Spectral Microscope Imaging System, Germany) was employed to probe the internal structure of fouling layer. The layer was imaged using a 10x or 20x objective and analyzed using Leika confocal software. The fluorescence of SYTO 63 was detected by excitation at 633 nm and emission at 650-760 nm (Red). Excitation at 543 nm and emission at 550-590 nm (light blue) were utilized to detect Con A conjugates. Nile Red was excited at 514 nm and emission collected over 630-700 nm (yellow). The FITC probe was detected by excitation at 488 nm and emission at 500-540 nm (green). The fluorescent intensity of SYTOX Blue was detected by excitation at 458 nm and emission at 460-500 nm (purple). The fluorescence of calcofluor white was determined by excitation at 405 nm and the emission width at 410-480 nm (blue). Both SYTO 63 and FITC were detected together and the others were detected individually.

IV. Results and Discussion (結果與討論)

CLSM images of fouling layer

Figure 1 presents CLSM images scanned at 5 μm above the membrane surface, representing the deposited layer on the membrane surface. In this scanned image, all six probed EPS were distributed in clusters over the fouling layer. The β-D-glucopyranose polysaccharides, lipids and proteins appeared to correspond closely to the cells (particularly the dead cells), revealing that these EPS may be mostly bound EPS to cell membranes. The presence of α-D-glucopyranose polysaccharides however is more weakly correlated with the cells, as noted for the other probed EPS, suggesting that it may contribute to the free EPS that is not tightly bound to the cell membrane.

Figure 2 displays the side-view images of CLSM, which combine three EPS (Calcofluor white, FITC and SYTO 63), underneath which is a 35μm thick membrane. This cross-sectional view indicates that the fouling layer has a thickness of 16–29 μm, and a very non-uniform spatial distribution. The β-D-glucopyranose polysaccharides were distributed over the fouling layer, while live cells were present as clusters in the layer.

Building fouling layer model

Using a series of CLSM images scanned on the fouling layer, the three dimensional distributions of nucleic acids and EPS can be generated by a method presented elsewhere [33.34]. The CLSM image was bileveled with a threshold value determined by Otsu's method. Then, the boundaries in the bileveled images were classified by connectivity and whether they were in the object or its complement. The connectivity of neighboring pixels in all analyses was set to four to detect the edges. When the boundaries were sketched, the isosurfaces were developed to determine the object's three-dimensional shape. The advancing-front algorithm is adopted to fill each region that is defined by the simplified polygonal surface model of the pores, with unstructured tetrahedral volumetric grids [35]. Over 10^6 grid cells were included in the mesh model to describe the interior of the fouling layer in **Fig. 3** (the central, porous layer). The void volume divided by the total volume obtained yielded the mean porosity of the organic fouling layer, which was estimated at 0.49.

The dark areas in the model represent the pore sites among the organic molecules, which were probed in the fouling layer. These can be blocked by other organic substances or inorganic particles. Accordingly, the flow field

that was simulated using the fouling layer model in **Fig. 3** represents the base case line to demonstrate the effects of blockage with additional inorganic particles on layer permeability. The mesh model of a fouling layer was placed perpendicular to an incoming Newtonian fluid of density ρ and viscosity μ, flowing at a uniform velocity of V from left end far away from membrane surface. **Figure 3** also shows the boundaries of the flow process in the computation.

Simulation of intra-layer flow field

The steady-state Navior-Stokes equations are the governing equations of the intra-layer and surrounding flow velocity of $\vec{u}$,

$$\left(\vec{u}'\cdot\nabla\right)\vec{u}'+\frac{P_0}{\rho V^2}\nabla P'=\frac{1}{Re}\nabla^2\vec{u}' \quad (1)$$

where $\vec{u}'=\vec{u}/V$, $P'=P/P_0$, $Re=\rho HV/\mu$., P_0 and H are the characteristic pressure and length, respectively. The boundary conditions are as follows.

$\vec{u}=\vec{V}$ at inlet surface (2a)

$\vec{u}=\vec{0}$ at solid's surfaces of fouling layer (2b)

In the calculations, tetrahedral grid cells in the computational domain were initially preprocessed using geometrical modeling mesh generation software, GAMBIT 2.0 (Fluent, Inc., USA). Then, the governing equations (Eq. 1) combined with boundary conditions (Eqs. 2a–b) were solved using FLUENT 6.1 software (Fluent, Inc., USA). The pressure-velocity coupling algorithm was SIMPLEC (Semi-Implicit Method for Pressure-Linked Equations-Consistent). The calculation was performed with a maximum relative error of 0.01%.

Figure 4 presents the contours of the cross-flow velocities over the planes 5, 10, 15 and 20 μm above the membrane surface. A non-uniform flow pattern is observed. The area-weighted mean pressure of the cross sections perpendicular to the flow direction was adopted to determine the mean pressure drop in the floc. Permeability was estimated from Darcy's law. The permeability of the fouling layer was defined as [(superficial velocity)(viscosity)/(pressure gradient)]=2.65×10^{-12} m^2.

The intrafloc flow pattern was displayed as a plot of the path lines. The trajectory function was defined as

$$\begin{cases}\dfrac{dx}{dt}=u_{p,X}(x,y,z,t)\\ \dfrac{dy}{dt}=u_{p,Y}(x,y,z,t)\\ \dfrac{dz}{dt}=u_{p,Z}(x,y,z,t)\end{cases}. \quad (3a\text{-}c)$$

Nine thousand fluid particles were initially released from the inlet plane and their paths through the fouling layer were individually monitored.

Figure 5 plots the path lines, colored according to the static pressure (gauge), measured in Pa. A very complex flow pattern is noticeable. Magnified views of a section of the flow field (A and B in **Fig. 5**) reveal that, because of the inter-connectivity of the neighboring pores, the flow direction may even be the reverse of that of the pressure gradient. The typically adopted one-dimensional fouling model is likely to be a poor approximation of the observed intra-layer flow field [32].

The path lines in **Fig. 5** yield an estimate of channel tortuosity in the fouling layer. The path lengths along all lines were averaged, and the average was divided by the thickness of the layer. This ratio was defined as the mean tortuosity τ, which was 1.42 for this fouling layer.

Effects of pore blockage on permeability

The known distributions of open pores over the layer must be used to determine how pore blockage affects the permeability of the fouling layer. When an image is transformed into a bileveled image, blobs (binary large objects) can be recognized and some features of the blobs, such as their areas and perimeters, can be quantified. The convex perimeter ($p_{C,p}$) is an approximate perimeter of the convex hull of a blob derived from the eight Feret diameters of the blob. Chu and Lee [33] noted that the so-called the "maximum convex perimeter method" determines the threshold value to describe the spatial distribution of small pores or interstices among the solid blobs in a bioaggregate matrix. The cross-sectional area and volume of each pore are A_p and V_p, respectively. Then, the shape of the pores is assumed to be circular so the pore diameter d_p is estimated as $\sqrt{\frac{4A_p}{\pi}}$.

Only one pore exists with a diameter of over 18.6 μm (**Fig. 6a**), but 42 pores have diameter > 8.8 μm (**Fig. 6b**). **Figure 7** plots pore volume as a function of pore diameter. Pores with diameter > 8.8 μm account for only about 15% of the porosity of the layer; the volume of the largest pore of size 18.6 μm was 0.67% of the total volume of the pores.

The identified pores were blocked artificially and the obtained fouling layer models (with blocked pores) were reconstructed and the intra-layer flow fields were recalculated. Then the mean permeability of the fouling layer was estimated. Blocking the pores with a diameter of over 12.7 μm reduces the porosity by 2.6%; the permeability was reduced from $2.68\text{x}10^{-12}$ to $2.26\text{x}10^{-12}$ m^2 - a 15.6% reduction. Further blocking the pores of diameters 12.7-8.8 μm reduced the permeability to $1.13\text{x}10^{-12}$ m^2, approximately by 58% of that of the unblocked biofouling layer. This observation is consistent with the note made by Wu *et al.* [36] that the largest pores in a porous medium are responsible for most of the advective flow.

Wu *et al.* [36] assumed that the bioaggregate interior could be modeled as a bundle of parallel straight round pipes, following the Hagen-Poiseuille law. That is, the mean permeability to which pores of size category j contributes is,

$$k_j=\frac{\varepsilon n_j d_j^4}{32\sum_1^N n_i d_i^2} \quad (4)$$

where the indices i and j are diameter category number n; that is, i=1 for n_1 pore diameter>18.6 μm; i=2 for n_2 diameters from 16.7 to 18.6 μm, and so on. The permeability associated with the individual pores in category

j satisfies $\left(k_j / n_j\right) \propto d_j^4$. The parameter k_j of the pores in each category can be determined from **Fig. 8**, and the number of pores can be estimated from the pore volume and the pore thickness, based on the assumption that the pores are cylindrical pipes. **Figure 9** shows that the calculated (k_j/n_j) value is approximated by a power-law in d_j^4. Therefore, the assumption that the interior pores can be treated as a bundle of parallel pipes is basically correct. However, the simulation results that are based on a complex structure (Fig. 3) reveal a higher permeability than is predicted by the Hagen-Poiseuille law (Eq. 4), perhaps because many intersects among various pores facilitate advection flow when some pores are blocked.

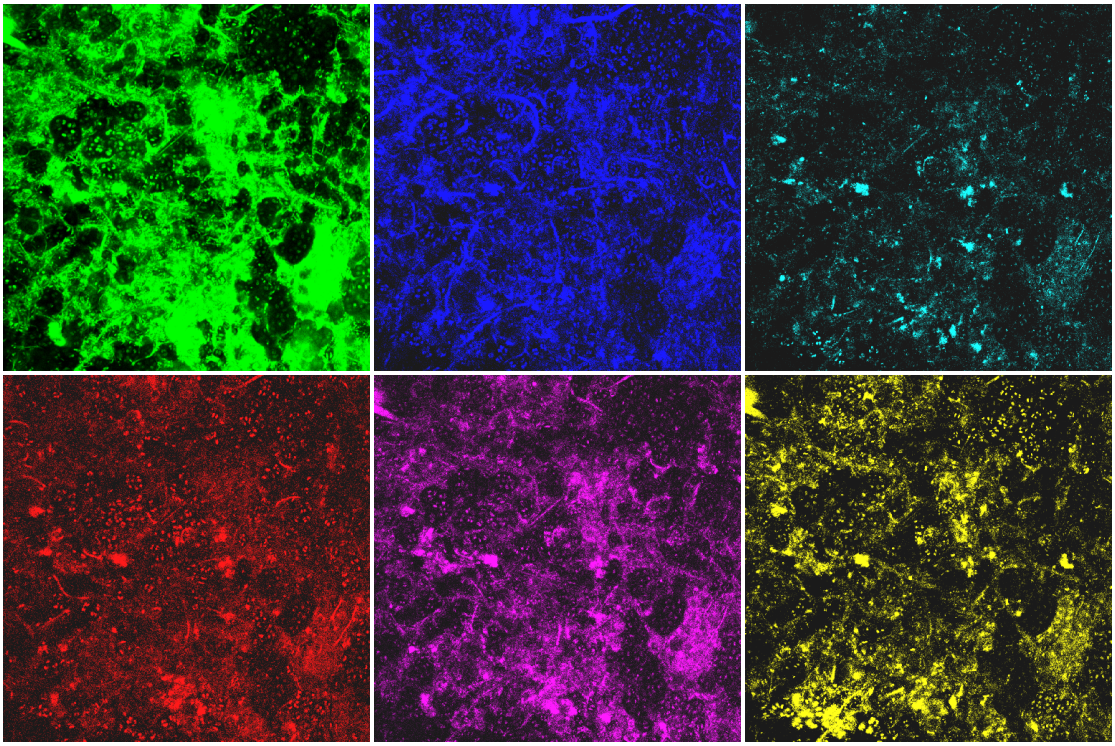

Figure 1 CLSM images scanned at 5 μm above membrane surface. Top view of fouling layer of image size 100 μm x 100 μm. Green: proteins, β-D-glucopyranose polysaccharides (blue), α-D-glucopyranose polysaccharides (light blue), red: total cells, purple: dead cells, yellow: lipids.

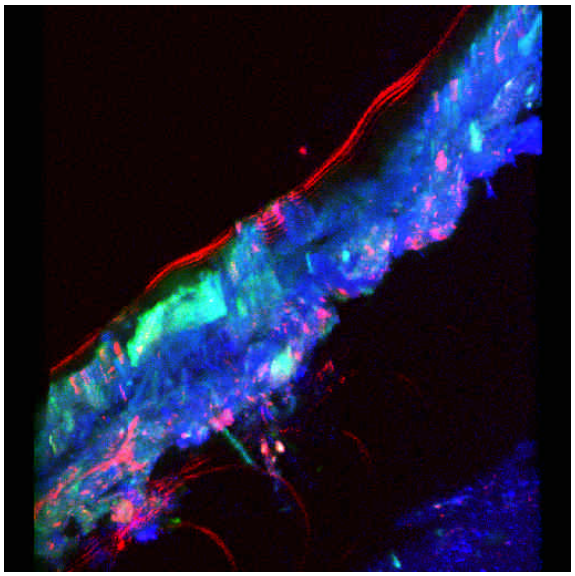

Figure 2 Cross-sectional view of fouling layer combining the CLSM images of proteins (green), total cells (red), and β-D-glucopyranose polysaccharides (blue). The size of image is of length 100 μm.

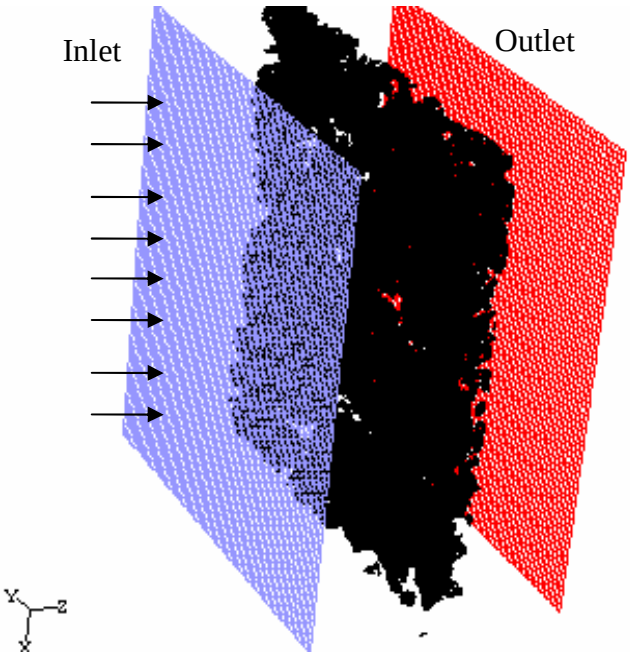

Figure 3. The computational domain of the present fouling layer model. The approaching velocity (*V*) is along the *z*-axis.

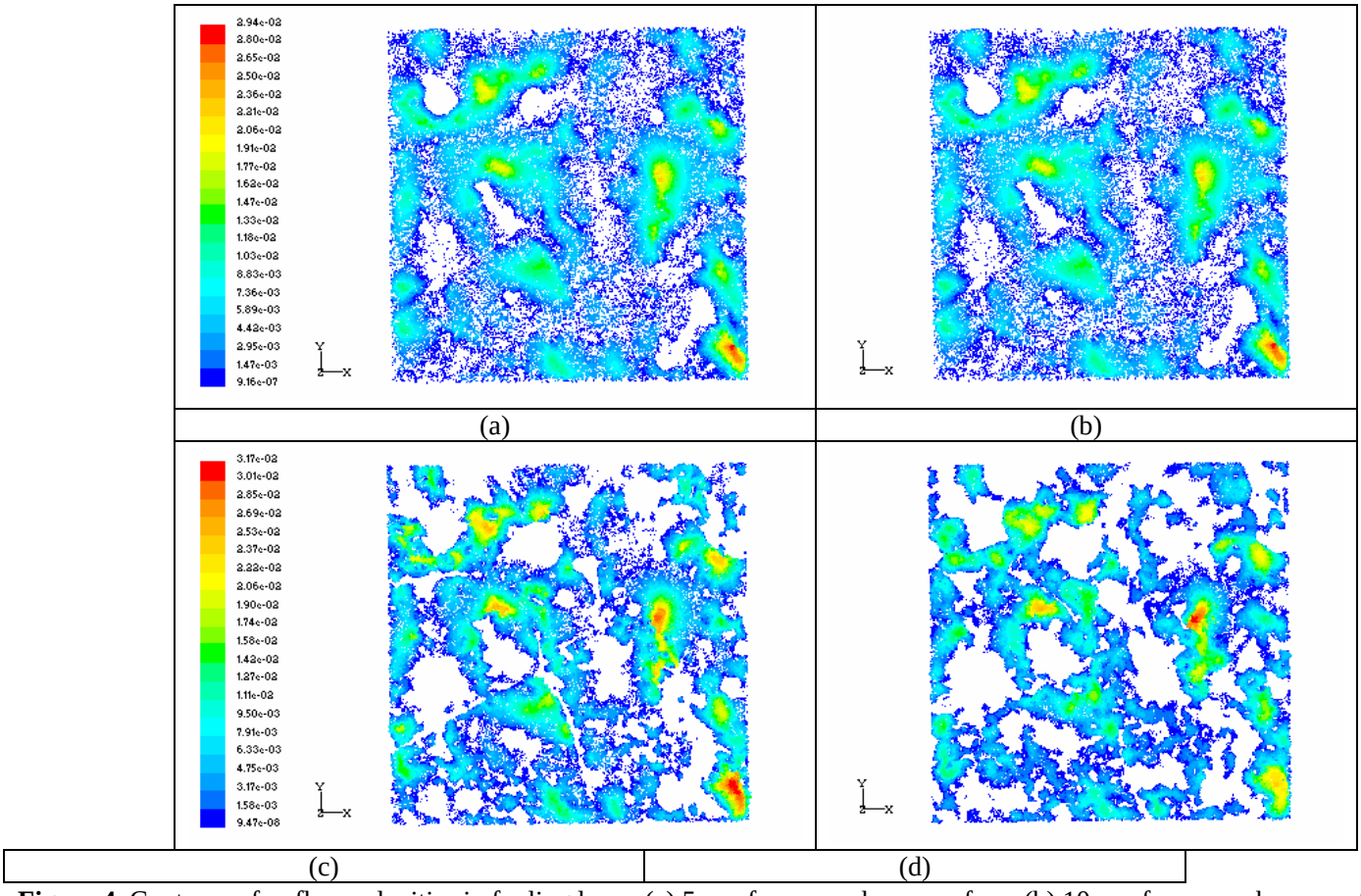

Figure 4. Contours of upflow velocities in fouling layer. (a) 5 μm from membrane surface; (b) 10 μm from membrane surface; (c) 15 μm from membrane surface; (d) 20 μm from membrane surface.

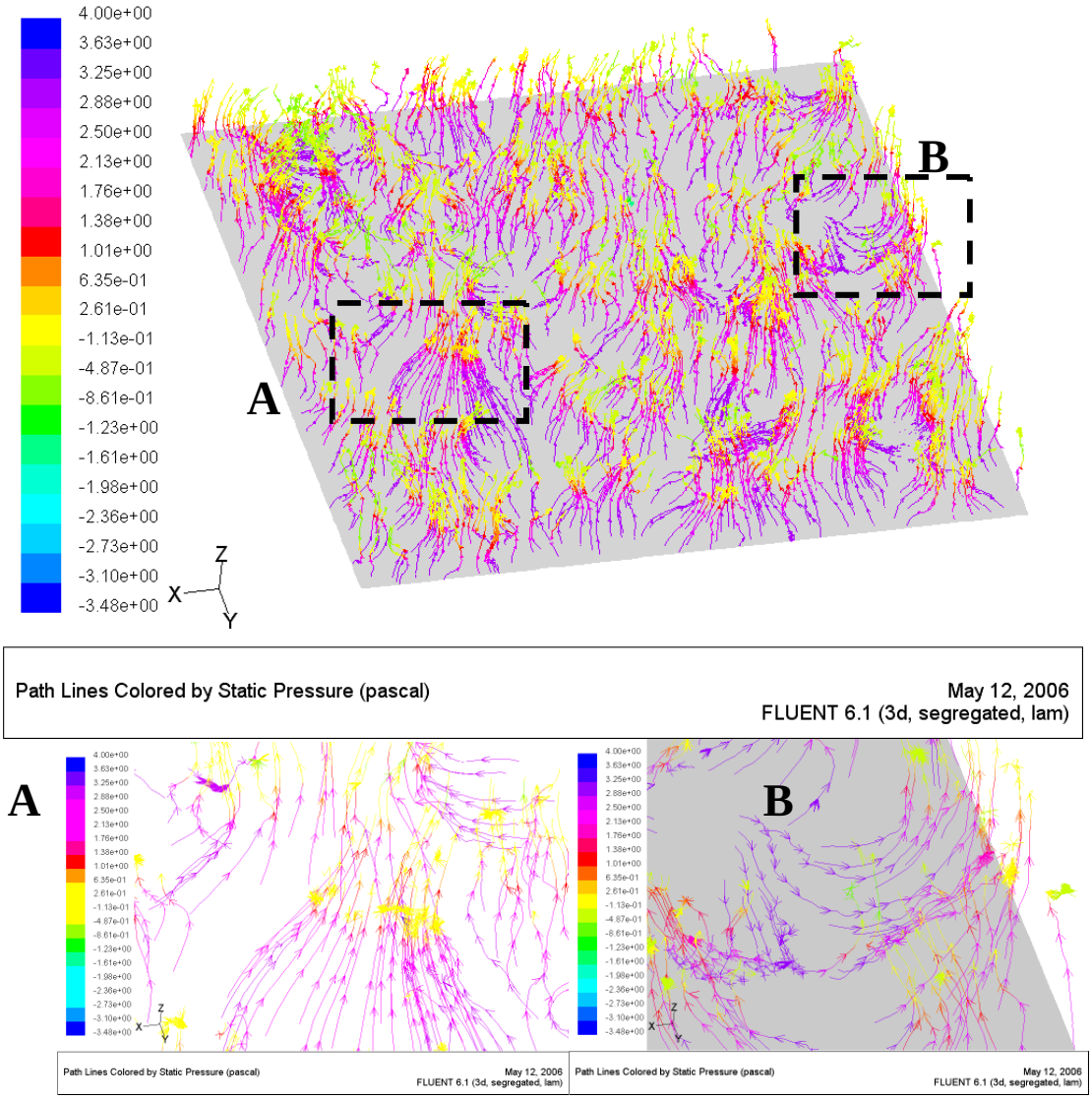

Figure 5. Path lines calculated based on the investigated fouling layer model. Regions A and B are magnified to reveal detailed flow field.

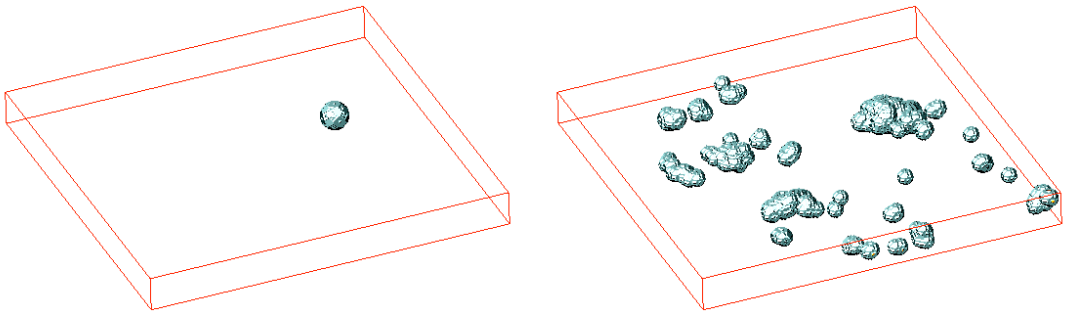

(a) (b)

Figure 6 The locations of internal pores inside the fouling layer. (a) Pore diameter ≥18.6 μm; (b) pore diameter ≥8.8 μm.

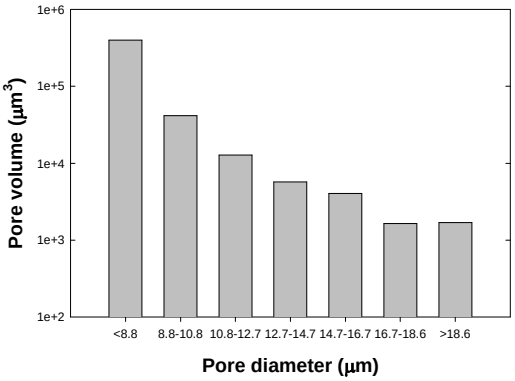

Figure 7 The volume versus diameter of internal pores inside the fouling layer.

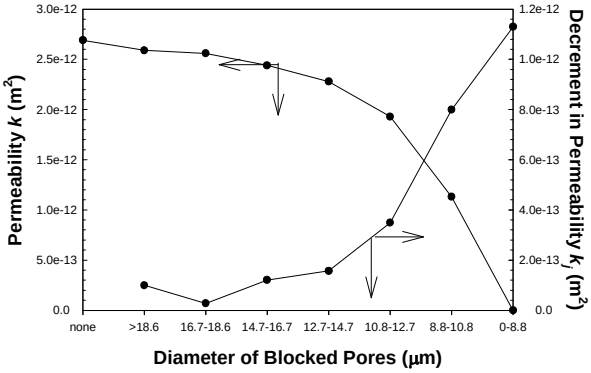

Figure 8 The permeability of fouling layer and decrement in permeability versus diameters of blocked pores inside fouling layer.

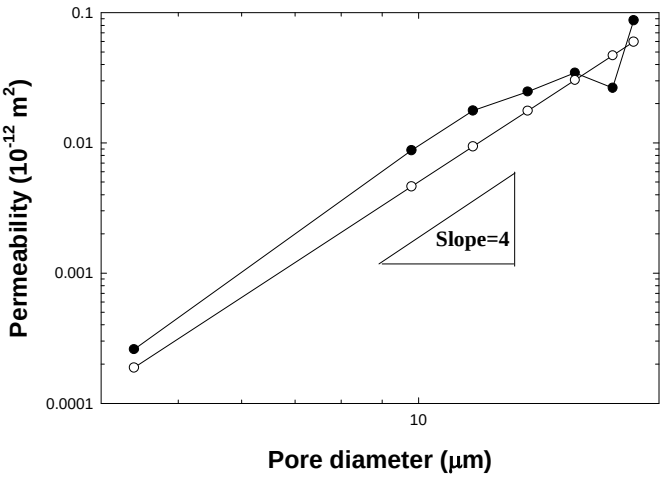

Figure 9 The permeability contributed by each pore in fouling layer versus pore diameter plot. Solid symbols: data from Fig. 8; open symbols: calculation based on eq. (4).

V. Reference (參考文獻)

[1] A. Ramesh, D. J. Lee, M. L. Wang, J. P. Hsu, R. S. Juang, K. J. Hwang, J. C. Liu, and S. J. Tseng, Biofouling in membrane bioreactor. Sep. Sci. Technol. 41 (2006) 1345-1370.

[2] P. Le-Clech, V. Chen, and A.G. Fane, Fouling in membrane bioreactors used in wastewater treatment –A review. J. Membr. Sci. (2006), doi:10.1016/j.memsci. 2006.08.019.

[3] K. Kimura, N. Yamato, H. Yamamura, and Y. Watanabe, Membrane fouling in pilot-scale membrane bioreactors (MBR2) treating municipal wastewater. Environ. Sci. Technol. 39 (2005) 6293-6299.

[4] H. Nagaoka, S. Yamanishi, and A. Miya, Modeling of biofouling by extracellular polymers in a membrane separation activated sludge system. Water Sci. Technol. 38 (1998) 497-504.

[5] H. Nagaoka, S. Ueda, and A. Miya, Influence of bacterial extracellular polymers on the membrane

separation activated sludge process. Water Sci. Technol. 34 (1996) 165-172.
[6] G. L. Leslie, R. P. Schneider, A. G. Fane, K. C. Marshall, and C. J. D. Fell, C. J. D. Fouling of a microfiltration membrane by two Gram-negative bacteria. Colloids Surf. A. 73 (1993) 165-178.
[7] G. G. Geesey, M. W. Stupy, P. J. Bremer, The dynamics of biofilms, Int. Biodetoriation Biodegradation 30 (1992) 135-154.
[8] I. S. Chang, P. Le-Clech, B. Jefferson and S. J. Judd. Membrane fouling in membrane bioreactors for wastewater treatment, J. Environ. Eng., 128 (2002) 1018-1029.
[9] B. D. Cho and A. G. Fane, Fouling transients in nominally sub-critical flux operation of a membrane bioreactor. J. Membr. Sci. 209 (2002) 391-403.
[10] I. S. Chang and C. H. Lee, Membrane filtration characteristics in membrane-coupled activated sludge systems-the effect of physiological states of activated sludge on membrane fouling. Desalination 120 (1998) 221-233.
[11] S. Rosenberger and M. Kraume, Filterability of activated sludge in membrane bioreactor. Desalination 146 (2002) 373-379.
[12] M. E. H. Rojas, M. R. van Kaam, S. Schetrite, and C. Albasim, Role and variations of supernatant compounds in submerged membrane bioreactor fouling. Desalination 179 (2005) 95-107.
[13] W. Lee, S. Kang, and H. S. Shin, Sludge characteristics and their contribution to microfiltration in submerged membrane bioreactors. J. Membr. Sci. 216 (2003) 217-227.
[14] E. H. Bouhabila, R. Ben Aim, and H. Buisson, Fouling characterization in membrane bioreactors. Separ. Purif. Technol. 22-23 (2001) 123-132.
[15] C. Wisniewski, and A. Grasmick, Floc size distribution in a membrane bioreactor and consequences for membrane fouling. Colloids Surf. A 138 (1998) 403-411.
[16] J. M. Lee, W. Y. Ahn, and C. H. Lee, Comparison of the filtration characteristics between attached and suspended growth microorganisms in submerged membrane bioreactor. Water Res. 35 (2001) 2435-2445.
[17] J. W. Cho, K. G. Song, S. H. Lee, and K. H, Ahn, Sequencing anoxic/anaerobic membrane bioreactor (SAM) pilot plant for advanced wastewater treatment. Desalination 178 (2005) 219-225.
[18] K. Stamatakis, and C. Tien, Cake formation and growth in cake filtration. Chem. Eng. Sci. 46 (1991) 1917-1933.
[19] M. A. Koenders, and R. J. Wakeman, The initial stages of compact formation from suspensions by filtration. Chem. Eng. Sci. 51 (1996) 3897-3908.
[20] B. Jefferson, A Brookes, P. Le-Clech and SJ Judd. Methods for understanding organic fouing in MBRs. Waste Sci. Technol., 49 (2004) 237-244.
[21] A .Brookes, S.J. Judd, E. Reid, E. Germain, S. Smith, H. Alvarez-Vazquez, P. Le-Clech, T. Stephenson, E. Turra, and B. Jefferson, Biomass characterization in membrane bioreactors, in: Proceedings of IMSTEC, Sydney, Australia (2003).
[22] H. Nakaoka and H. Nemoto, Influence of extracellular polymeric substances on nitrogen removal in an intermittently aerated membrane bioreactor. Waste Sci. Technol., 51 (2005) 151-158.
[23] B. Jesjean, S. Rosenberfer, C. Laabs, M. Jekel, R. Gnirss and G. Amy, Correlation between membrane fouling and soluble/colloidal organic substances in membrane bioreactors for municipal wastewater treatment, Water Sci. Technol., 51 (2005) 1-8.
[24] S. Rosenberger, H. Evenblij, S. te Poele, T. Wintgens, and C. Laabs, The importance of liquid phase analyses to understand fouling in membrane assisted activated sludge processes-six case studies of different European research groups. J. Membr. Sci. 263 (2005) 113-126.
[25] H. Evenblij, S. Geilvoet, J. Van der Graaf, and H. F. Van der Roest, Filtration characterisation for assessing MBR performance: three cases compared. Desalination 178 (2005) 115-124.
[26] K. Tarnacki, S. Lyko, T. Wintgens, T. Melin, and F. Natau. Impact of extracellular polymeric substances on the filterability of activated sludge in membrane bioreactors for landfill treatment. Desalination 179 (2005) 181-190.
[27] T. R. Neu, and J. R. Lawrence, Lectin-binding analysis in biofilm system, Method Enzymol., 310 (1999) 145-152.
[28] M. Strathmann, J. Wingender, and H. C. Flemming, Application of fluorescently labeled lectins for the visualization and biochemical characterization of polysaccharides in biofilms of Pseudomonas Aeruginosa, J. Microbiol. Methods, 50 (2002) 237-248.
[29] M. A. Yun, K. M. Yeon, J. S. Park, C. H. Lee, J. Chun, and D. J. Lim, Characterization of biofilm structure and its effect on membrane permeability in MBR for dye wastewater treatment, Water Res., 40 (2006) 45-52.
[30] H. Y. Kim, K. M. Yeon, C. H. Lee, S. H. Lee, and T. Swaminathan, Biofilm structure and extracellular polymeric substances in low and high oxygen bioreactors, Sep. Sci. Technol., 41 (2006) 1213-1230.
[31] M. Y. Chen, D. J. Lee, and J. Y. Lai, Excellular polymeric substances in fouling layer. Sep. Sci. Technol., 41 (2006) 1345-1370.
[32] M. Y. Chen, D. J. Lee, Z. Yang, X. F. Peng, and J. Y. Lai. Fluorecent staining for study of extracellular polymeric substances in membrane biofouling layers. Environ. Sci. Technol., accepted.
[33] C. P. Chu, and D. J. Lee, Bilevel thresholding of image of sludge flocs. Environ. Sci. Technol., 38 (2004) 1161-1169.
[34] C. P. Chu, and D. J. Lee, Effects of pore geometry on intrafloc flow. J. Chem. Inst. Chem. Engrs. 35 (2004) 659-666.
[35] C. P. Chu, and D. J. Lee, Multiscale structure of biological flocs. Chem. Eng. Sci. 59 (2004) 1875-1883.
[36] R. M. Wu, D. J. Lee, and P. J. He. Estimation of floc permeability and porosity. J. Chin. Inst. Chem. Engrs. 34 (2003) 275-280.

出國報告書

台大化工李篤中

本次在國科會計畫 NSC95-2221-E-002-385 之支持下，前往新加坡進行國際合作參訪，行程自 2006 年 8 月 19 日至 2006 年 9 月 2 日止，共計 15 日，國科會計劃補助 14 日生活費及機票費，餘自付。

謹此將行程簡述如下：

8 月 19 日　本日搭乘長榮航空 BR225 赴新，當日進住新加坡南洋理工大學 Nanyang Executive centre（NEC）。

8 月 20 日　此日休假。

8 月 21 日　本日赴新加坡南洋理工大學人事室報到。在新期間本人受聘為其訪問教授，負責參與其一國家型計畫，並定期與專案人員討論進度。

8 月 22 日　本計畫為一延續型計畫，本日與南洋理工大學 IESE 工作組繼續討論進行下一波專利“地雷”佈置事宜。目地在於將關鍵技術完全包圍以搶得日後市場競爭力。

8 月 23 日　本日起再擔任其 IESE 博士生課程中之“進階密集課程”講師，進行一連三日之密集課程講授。本日之課程主題為“Membrane bioreactor: practice and design”，共六小時，有博士生及政府官員約 30 人參加。

8 月 24 日　本日繼續進行密集課程之二，主題為“Aerobic granules process: fundamentals and applications”，亦為六小時課程。

8 月 25 日　本日繼續進行密集課程之三，主題為“Landfill bioreactor: total

solution of leachate and solid waste pollution”，亦為六小時課程。

8 月 26 日及 27 日　此二日休假。

8 月 28 日　本日起參加新加坡舉辦之“2006 Bioenergy Outlook”，本人受邀為其大會主辦人之一，並主持其中 Energy from biomass 一場之發表與討論。

8 月 29 日　本日繼續參加前一日之學術會議，並參加其會後之圓桌會議。

8 月 30 日　本日赴新加坡國立大學化工系訪問，並與工學院副院長 Way CH 完成一篇共同合作課題之論文寫作。

8 月 31 日　本日休息。

9 月 1 日　此日休假。

9 月 2 日　本日搭乘 BR226 返台。